

Magnetotransport and electronic band structure of EuNi_2As_2 antiferromagnet

Faheem Gul¹,^{*} Mane Sahakyan¹, Orest Pavlosiuk¹ and Piotr Wiśniewski^{1, *}

¹*Institute of Low Temperature and Structure Research, Polish Academy of Sciences, Wrocław, Poland*

(Dated: July 7, 2026)

We investigated the magnetotransport properties of single-crystals of tetragonal van der Waals compound EuNi_2As_2 , that orders antiferromagnetically below 14.6 K in an incommensurate helical structure. Metamagnetic transitions are revealed by the magnetization measured in the magnetic field applied transverse to the axis of the helix, and are clearly reflected in the magnetoresistance. Overall, the magnetoresistance is small, but shows complex changes with the temperature, the strength, and the angle of the applied magnetic field. In magnetically ordered state, magnetoresistance shows prominent anomalies related to the metamagnetic transitions. For temperatures above the Néel point the negative magnetoresistance can be modeled very well with de Gennes-Friedel mechanism of the spin-disorder-scattering reduction. Hall resistivity data indicate hole-dominated multi-band conductivity in antiferromagnetic state and single-band one above the Néel temperature, with carrier concentrations of the order of 10^{22}cm^{-3} . This metallic character of the compound seems to obscure the plausible topological contribution to the Hall resistivity. Our *ab-initio* calculations of electronic band structure showed that the electronic structure changes very strongly upon magnetic ordering, but the density of states at the Fermi level differs by a factor smaller than two, in agreement with experimental Hall resistivity data. Meaningful changes in the density of states, magnetic moments, and screening length of Eu-4*f* orbitals are discussed in terms of the effects of Hubbard corrections.

I. INTRODUCTION

Research on the complex interplay of magnetism and electronic band structure has a long history, but has been strongly rejuvenated with the discovery of topological insulators and semimetals [1]. Eu-based compounds provide fertile ground for this endeavor, mainly due to the strong magnetic moments of Eu^{2+} ion and lack of a crystalline-field effect [2]. Recent studies of several Eu-based systems of 1:2:2 stoichiometry, such as EuCd_2As_2 [3, 4], EuCd_2Sb_2 [5, 6], EuZn_2Sb_2 [7], EuIn_2As_2 [8], revealed that the magnetic structure can induce or significantly alter topologically non-trivial electronic band structure.

Interestingly, all these compounds exhibit a pronounced topological Hall effect (THE). In EuCd_2As_2 and EuCd_2Sb_2 , both Weyl nodes and scalar chirality of non-coplanar spins induce a Berry curvature that gives rise to THE. In EuZn_2Sb_2 and EuIn_2As_2 solely the second mechanism plays a role, although with various backgrounds: in the former compound, the spin chirality occurs within the domain wall, whereas in the latter, it is brought by the magnetic field applied to the helical magnetic structure [8, 9].

Another europium compound, but from the 1:1:1 family, namely, EuCuAs , brought additional motivation for this work. It also has the incommensurate helical magnetic structure [10]. Such a magnetic structure breaks an inversion and time reversal symmetry, which induces Weyl nodes leading, in turn, to the rise of the topological Hall effect [10, 11]. All the mentioned above

compounds exhibit antiferromagnetism due to Ruderman–Kittel–Kasuya–Yosida interactions and they are semimetals with carrier concentrations of the order of magnitude of 10^{19}cm^{-3} .

Upon looking for other helical antiferromagnets, that might by exhibiting THE, we noticed the EuNi_2As_2 compound crystallizing in a body-centered tetragonal ThCr_2Si_2 -type structure ($I4/mmm$ space group) [12, 13]. Resistivity measurement has shown that the system is more metallic than all previously mentioned compounds. It orders antiferromagnetically below the Néel temperature $T_N=14.6\text{K}$. The neutron powder-diffraction analysis has revealed that it has an incommensurate helical magnetic structure with spins stacked ferromagnetically in the *ab*-planes and arranged helically around the *c*-axis, with the (0, 0, 0.92) propagation vector [13]. Due to these interesting features, the study of magnetotransport properties of this compound seemed indispensable. Therefore we grew single crystals of EuNi_2As_2 , and present below the results of performed on them magnetic and magnetotransport measurements.

There was a recent theoretical report in which, the results of *ab-initio* density-functional theory (DFT), using a simple GGA approximation [14], have been presented. They included the electronic and magnetic properties of $\text{EuFe}_{2-x}\text{Ni}_x\text{As}_2$ solid solution, but with an emphasis on the effect of Ni substitution on the possible emergence of superconductivity in the system.

Here, we also present the results of fully relativistic DFT calculations of the band structure of the compound, but performed in a more extended way compared to that described in [14] (focusing on the effects of Hubbard term corrections), including dispersions of energy bands, densities of states, magnetic moments and screening length of Eu-4*f* orbitals.

* e-mail: p.wisniewski@intibs.pl

II. METHODS

Experimental

The high-quality single crystals of EuNi_2As_2 were grown using the Bi flux (for details see Supplemental Material [15]). The energy-dispersive x-ray spectroscopy (EDS) using NanoSEM 230 (FEI Nova) scanning electron microscope equipped with an EDAX Genesis XM4 spectrometer was employed to examine their chemical composition.

The quality and orientation of the single crystals were determined by Laue back-scattering x-ray diffraction using the LAUE-COS (Proto Mfg.) system. Magnetic properties measurements were carried out with the SQUID magnetometer (MPMS-XL, Quantum Design). Electrical transport measurements were performed on the PPMS (Quantum Design) platform. The bar-shaped samples were cut from single crystals for the electrical transport measurements, which we carried out using the standard four-probe technique. Electrical contacts were prepared with 100 μm -thick silver wires attached to the sample with silver paste. The heat capacity was measured on the PPMS platform by the relaxation method.

Computational details

We investigated the electronic band structure of EuNi_2As_2 in the following steps: (i) first, we performed a unit cell optimization on the lattice parameters using the Pseudo Potential Projector Augmented Wave (PP-PAW) approach (VASP software version 5.4.4) [16]. As starting parameters, we took the lattice parameters reported for EuNi_2As_2 in literature: $a=0.4101$ nm and $c=1.0046$ nm [13]. The optimization was performed with Perdew–Burke–Ernzerhof (PBE) generalized gradient (GGA) exchange–correlation functional [17]. The relaxed lattice parameters of EuNi_2As_2 $a=0.4001$ nm, $c=1.0297$ nm, are comparable to the previously reported [14]. Thus, the optimized unit cell volume was reduced by 2.47%.

(ii) The DFT calculations of electronic band structure of EuNi_2As_2 were performed by Full-Potential Linearized Augmented Plane-Wave plus local orbitals (FP-LAPW+lo) method [18]. The DFT calculations have been done using the ELK computational code (version 8.8.26) [19], employing the local spin density approximation with the inclusion of Coulomb correlations (LSDA+U) [20]. The tetrahedron method of k integration was applied for self-consistent calculations with the $(10 \times 10 \times 4)k$ -mesh of the Brillouin zone. The plane wave cut-off was determined such that $R^{MT} \times |G+k|_{max} = 9.0$, with R^{MT} denotes the average atomic radius and G_{max} represents the maximum wave vector value. Muffin-tin geometrically optimized sphere radii were as follows: $R_{\text{Eu}}^{MT} = 0.148$ nm, $R_{\text{Ni}}^{MT} = 0.117$ nm, and $R_{\text{As}}^{MT} = 0.117$ nm. The stability requirement for self-consistency calculations was set to the total energy variation within 10^{-5} eV and for the Kohn–Sham potential 10^{-7} eV.

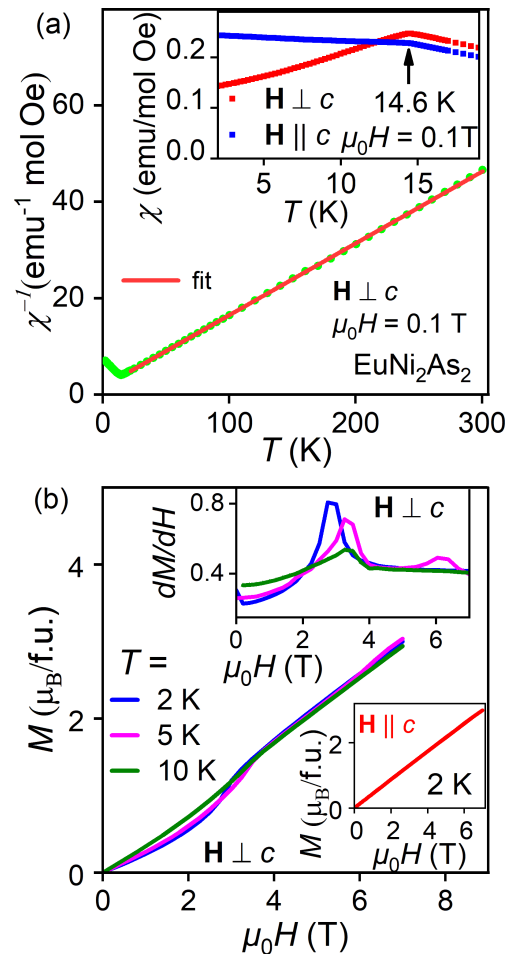


FIG. 1. (a) The temperature dependence of the inverse of susceptibility. The inset shows $\chi^{-1}(T)$ at $T < 20$ K, for both $\mathbf{H} \perp c$ and $\mathbf{H} \parallel c$. (b) The field dependence of the magnetization M for $\mathbf{H} \perp c$ and, in lower inset - for $\mathbf{H} \parallel c$, the upper inset shows derivative dM/dH for $\mathbf{H} \perp c$, in units of $\mu_B/(T \text{ f.u.})$.

(iii) Calculations were performed with the inclusion of the spin-orbit coupling and spin polarization effects, accounting for Eu^{2+} moments in an incommensurate antiferromagnetic helical structure with a magnetic propagation vector $k = (0, 0, 0.92)$ determined by neutron diffraction experiments [13].

III. MAGNETIC PROPERTIES

Temperature dependence of the inverse of the magnetic susceptibility, $\chi^{-1}(T)$, and magnetization as a function of magnetic field, $M(H)$ are shown in Fig. 1.

The Curie-Weiss law: $\chi^{-1} = (T - \theta_p)/C$ was fitted to the data collected in the magnetic field $\mu_0 H = 0.1$ T, applied perpendicular to the c -axis, at temperatures between 40 K and 300 K, as shown in Fig. 1(a). Here $C = \mu_0 N \mu_{\text{eff}}^2 / 3k_B$ is the Curie parameter and θ_p is the paramagnetic Curie-Weiss temperature. The paramagnetic

ters obtained from the fit are as follows: $\theta_p = -11$ K and the effective magnetic moment, $\mu_{\text{eff}} = 7.33 \mu_B$. The μ_{eff} is slightly lower than the theoretical value for Eu^{2+} ($7.94 \mu_B$), while θ_p is close to the previously reported [12]. $\chi(T)$ measured in $\mu_0 H = 0.1$ T for two field directions: $\mathbf{H} \parallel c$ and $\mathbf{H} \perp c$ -axis, confirms an AFM ordering below $T_N = 14.6$ K, consistent with previous reports [12, 13] (see the inset of Fig. 1(a)).

$M(H)$ was also measured for both directions: $\mathbf{H} \perp c$ and $\mathbf{H} \parallel c$, as shown in Fig. 1(b) and its lower inset, respectively. It attains $\approx 3 \mu_B/\text{f.u.}$ at 7 T, for both field directions. Metamagnetic transitions (MMTs) are visible for $\mathbf{H} \perp c$. The transition at ≈ 3 T becomes gradually less pronounced upon increasing T from 2 to 10 K, but the second noticeable transition occurs at $T = 5$ K, just above $\mu_0 H = 6$ T, clearly revealed by dM/dH presented in the upper inset of Fig. 1(b). On the other hand, $M(H)$ in $\mathbf{H} \parallel c$ is linear, as shown in the lower inset, without noticeable trace of transitions. These observations are in accord with the report of Sangeetha et al. [12].

IV. MAGNETOTRANSPORT PROPERTIES

The magnetic field dependence of resistivity, ρ_{xx} , of EuNi_2As_2 is shown in Fig. 2 for various temperatures ranging from $T = 2$ to 50 K, in different configurations. Figs. 2(a, b and c) show $\rho_{xx}(H)$ for field applied at various angles, at 2, 5 and 10 K respectively. The experimental configuration was such that \mathbf{H} remained perpendicular to the current, \mathbf{j} , but was rotated from perpendicular to parallel to the c -axis, as schematically depicted in inset to Fig. 2(a). The $\rho_{xx}(H)$ increases in the weak magnetic fields for given temperatures with a hump close to $\mu_0 H = 3$ T for 2 K that shifts slightly toward higher field with increasing temperature, followed by a decline for 5 and 10 K. Interestingly, for 5 K, another hump arises in the magnetic field above 6 T. These anomalies in $\rho_{xx}(H)$ align with the MMTs reflected in $M(H)$, for $\mathbf{H} \perp c$, and vanish as \mathbf{H} rotates toward c -axis.

The angular dependence of ρ_{xx} at $T = 5$ K, for various magnetic fields is shown in Fig. 3. The geometry of measurement was similar to that shown in Fig. 2(a), however, this time \mathbf{H} was rotated continuously by angle θ towards c -axis, as shown in inset to Fig. 3, while the field strength and the temperature were fixed. Interestingly, $\rho_{xx}(T = 5 \text{ K})$ at $|\theta| \approx 65^\circ$ for all of the fields collapses to nearly identical value. This, means that the magnetoresistance is negligibly small at that angle or, in other words, a compensation occurs of the mechanisms inducing negative and positive magnetoresistance.

To visualize the field variation of ρ_{xx} for ($\mathbf{H} \parallel c \perp \mathbf{j}$), we calculated the magnetoresistance using the relation: $\text{MR} = [\rho(H)/\rho(0)] - 1$. For $T = 2$ K, MR is positive, reaching 1.5% in $\mu_0 H = 9$ T as shown in Fig. 2(d). For $T = 4$ K and above, it turns negative, and becomes the most pronounced (-11.2% for 9 T) as 15 K is reached, just above T_N . It then starts to increase with increasing tempera-

ture, up to -2.5% at 50 K.

The negative MR seems due to reduction of the spin-disorder scattering, a mechanism described by the de Gennes and Friedel [21]. It associates the magnetic field dependence of paramagnet's resistivity with its magnetization as: $\rho_{xx}(H) \propto (1 - M^2)$ [22]. We approximated $M(H)$ with the Brillouin function and achieved excellent fitting to the experimental $\rho_{xx}(H)$ data collected at $15 \text{ K} \leq T \leq 50 \text{ K}$, as shown in Fig. 4. Details of that model fitting and obtained parameters are presented in Supplemental Materials [15].

Several compounds have been reported that display the THE due to the spin chirality, emerging at the MMTs. The chiral spin structure can add Berry phase to the wavefunctions of conduction electrons, which leads to phenomena like THE [11, 23]. However, for our samples of EuNi_2As_2 , the measurements of Hall resistivity for the field direction, in which MMTs were observed are virtually impossible. This is because the single crystals grew very thin in c -direction and therefore we could not prepare the sample with the voltage contacts spanning along c -axis.

The magnetic field dependence of the Hall resistivity, ρ_{xy} , for various temperatures from $T = 2$ to 50 K, in fields up to 9 T, is displayed in Fig. 5. The slightly curvilinear $\rho_{xy}(H)$ is observed for $T = 2$ K and 4 K, up to the highest applied magnetic field. Such an observation reveals the presence of more than one band crossing the Fermi level. For higher temperatures, namely ≥ 4 K, linear fits of $\rho_{xy}(H) = \mu_0 H / (en)$, were performed to estimate the carrier concentration n (e is the elementary charge). A positive ordinary Hall coefficient $(en)^{-1}$ indicates that the holes are dominant charge carriers in EuNi_2As_2 . The carrier density is of the order of 10^{22} cm^{-3} , and changes moderately with increasing temperature as shown in the inset of Fig. 5. This reconfirms metallic nature of this compound, in accordance with its very small Hall resistivity. Unfortunately this impedes observation of THE, which usually bring out the topological ρ_{xy}^T being usually only a few percent of the total ρ_{xy} [7].

V. ELECTRONIC STRUCTURE

There are no spectroscopic data available for EuNi_2As_2 , therefore instead of the commonly used value of Coulomb correlation potential, $U = 8$ eV for Eu^{2+} [24–26], we used several values of U from 5 to 8 eV at intervals of 0.5 eV, including double counting correction in fully localized limit (FLL) [27]. It occurred, $U = 5$ eV was the most suitable value with the least total energy among the rest, with a modest difference in the electronic band calculations. Hence, all the subsequent calculations were performed for this value of U . The characteristic features of band structure for the considered values of U are presented in Tab. I.

The electronic band structure for $U = 5$ eV in the paramagnetic state is shown in Fig. 6(a), with a finite num-

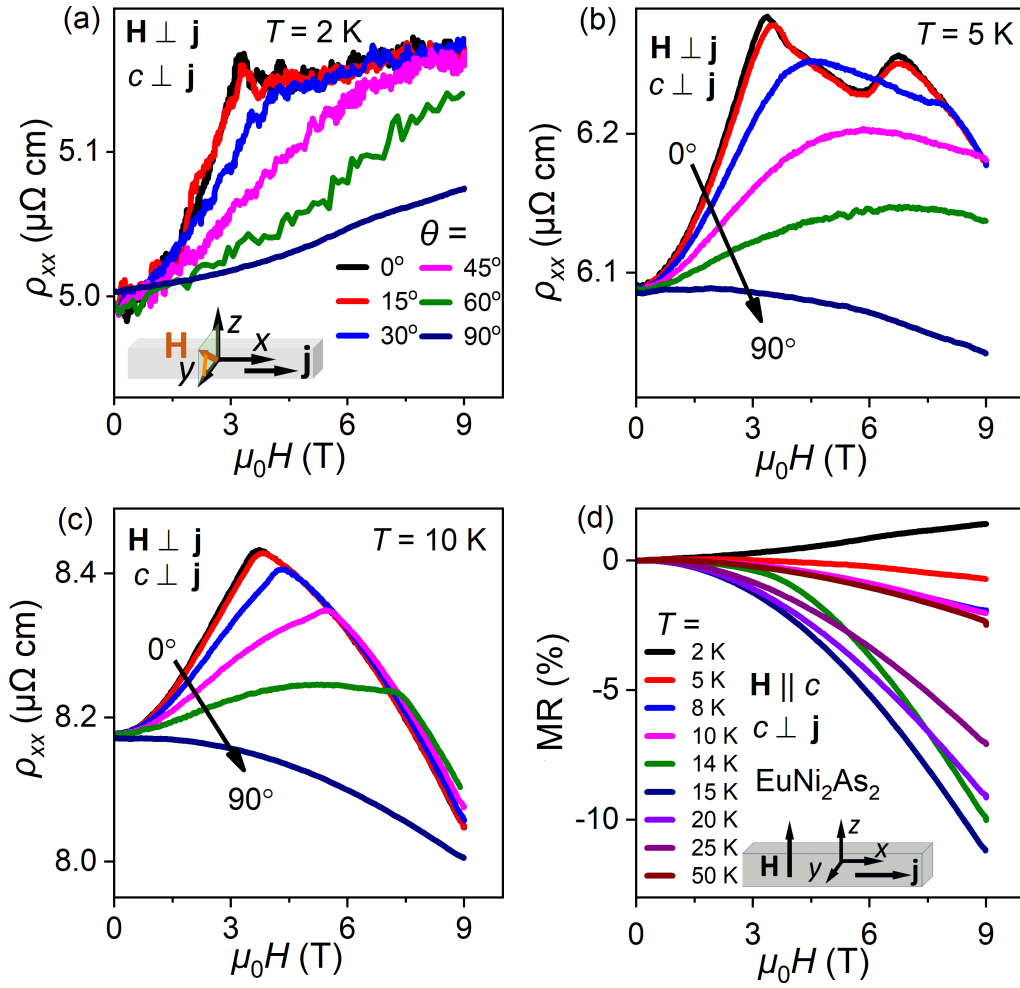


FIG. 2. The magnetic field dependence of resistivity in different configurations for (a) $T=2$ K, (b) 5 K and (c) 10 K. The color scheme for (b) and (c) is identical to (a). (d) The magnetoresistance for various temperatures above and below T_N .

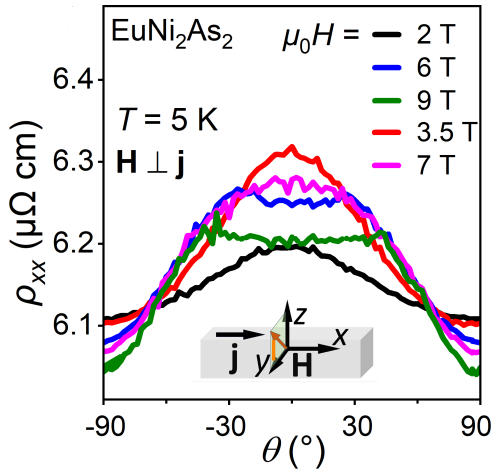


FIG. 3. Field-angle dependence of longitudinal resistivity at 5 K, for various magnetic fields.

ber of hole and electronic pockets. Fig. 6(b) displays the

Brillouin zone sketch of EuNi_2As_2 . The electronic band structure for the helical AFM state is shown in Fig. 6(c). In the paramagnetic region four 2-fold degenerate bands cross the Fermi surface. This degeneracy is lifted in the AFM state, where 8 bands cross the Fermi surface. Furthermore, the band structures with various U values for the helical AFM state were almost identical (comparison not shown here for simplicity's sake) near the Fermi level, indicating the dominant metallic behavior. The number of electron and hole pockets contributes to the total conductivity through the Fermi level, E_F . We observe multiple Dirac-like cones in the helical AFM phase in the close vicinity of E_F marked with arrows in Figs. 6(d-f). However, the contribution of topologically nontrivial states is not detected in our transport measurements, most likely overwhelmed by the contributions from trivial bands.

To gain a deeper understanding of the electronic band structure, we also calculated the density of states (DOS). The partial (PDOS), interstitial (IDOS), and total (DOS) are illustrated in Fig. 7 for paramagnetic and ordered phases. The Eu-4*f* level lies above E_F in the paramag-

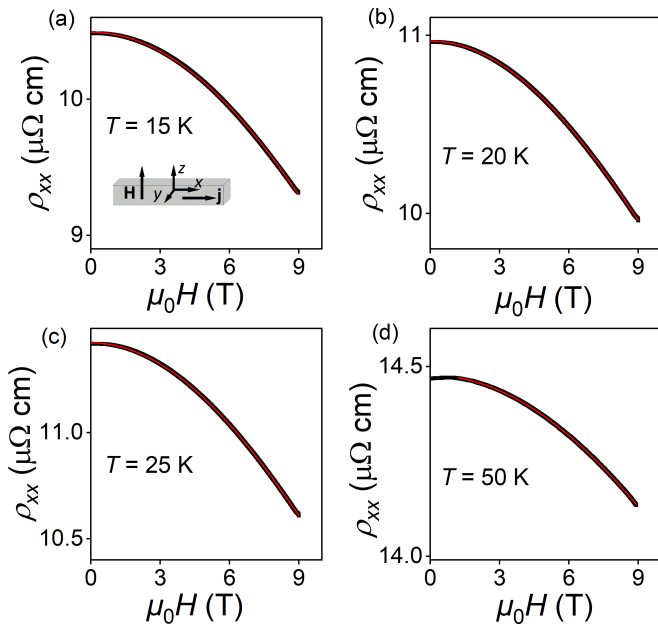


FIG. 4. The magnetic field dependence of the longitudinal resistivity for (a) $T = 15$ K, (b) 20 K, (c) 25 K, and (d) 50 K. The red solid lines show the fits of the de Gennes-Friedel model, detailed explanation and fit parameters are presented in Supplemental Material [15]).

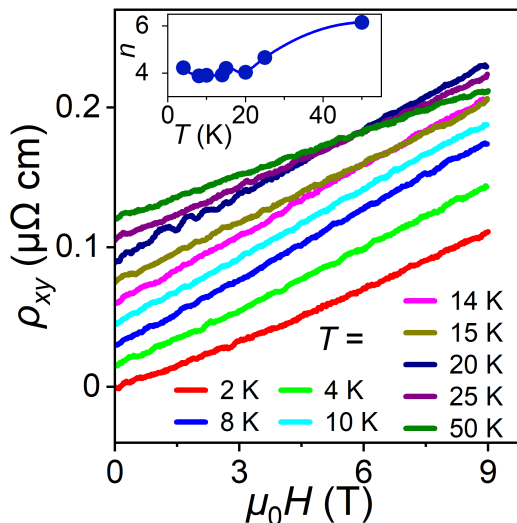


FIG. 5. Magnetic field dependence of Hall resistivity for temperatures ranging from $T = 2$ to 50 K (data are offset for clarity's sake). Inset shows charge carrier concentration, n , in 10^{22} cm^{-3} units.

netic state and shifts below E_F in the ordered phase. The $4f$ bands exhibit a minor contribution at E_F , while spiking well below the Fermi level, thus resulting in weak hybridization with Ni- $3d$ states. The FLL correction within the LSDA+ U method clearly results in a greater degree of f -electrons' localization than the GGA method calculations reported by Tran et al. [14]. Whereas the Ni- $3d$ band is the major contributor to the total conductiv-

ity at the Fermi surface, the As- $4p$ band negligibly contributes to the total conductivity, as shown in Fig. 7(b). The IDOS and DOS are depicted in the lower panel of Fig. 7(a). Interestingly, 20% of DOS value at the Fermi level is coming from the contribution of IDOS. DOS(E_F) in the paramagnetic and helical AFM phases changes from 3.3 to 6.13 states/(eV f.u.), respectively, which reflects the modest change in carrier concentrations between the two regions.

The spin-polarized data of all calculations support the magnetic order and show that the essential contribution to the magnetic moment should come from Eu- $4f$ ions. The estimated total magnetic moments presented in Tab. I are comparable to the experimental value of $6.75(6) \mu_B/\text{Eu}$ reported earlier [13]. Using the screened Coulomb interaction in the form of a Yukawa potential proposed by Norman et al. [28], by choosing U and J individually, we obtained the screening length values for $4f$ shells. (Tab. I). The small values of the screening length of $4f$ orbitals of Eu^{2+} are due to the fact that they are deeply shielded by the filled $5s$ and $5p$ orbitals, which in turn shield the $4f$ electrons from their surrounding environment. We observe that at the fixed $J = 0.8 \text{ eV}$, the increasing Hubbard U term from 5 to 8 eV results in a slight growth in the magnetic moments from 6.98 to $7.041 \mu_B$, while the screening length decreases. We observe the LSDA+ U moments in the limit of screening length. We note that by gradually decreasing the λ parameter, one increases the localization of the $4f$ electrons. The similar behavior was also found in the case of $5f$ shells in U, Np, Pu-based actinide compounds [29].

VI. CONCLUSION AND SUMMARY

We grew and characterized single crystals of EuNi_2As_2 . We remeasured their magnetic properties, which reaffirmed that the magnetic order takes place below $T_N = 14.5 \text{ K}$ and the effective magnetic moment is $7.33 \mu_B$. We measured and analyzed the transverse magnetoresistance for different orientations of the applied magnetic field. The MR for $\mathbf{H} \parallel c$ -axis is about few percent and negative at low temperatures, which for $T > T_N$ we ascribe to the de Gennes-Friedel mechanism. The anomalies in $\rho_{xx}(H)$ for $\mathbf{H} \perp c$ -axis corresponds well to MMTs, which are observed in magnetization for the same direction of the applied magnetic field. Occurrence of such anomalies in MR are usually ascribed to the Berry curvature in real space due to the spin chirality, and they are accompanied by THE. Unfortunately, the configuration of Hall measurement with $\mathbf{H} \perp c$ is inaccessible for our very thin in c -direction samples. Only cutting crystals with focused ion beam could allow preparation of the sample in such configuration, but nevertheless we doubt, that THE could be observed in our metallic compound.

Further, by analyzing the Hall resistivity measured in $\mathbf{H} \parallel c$, we found that multiple bands contribute to

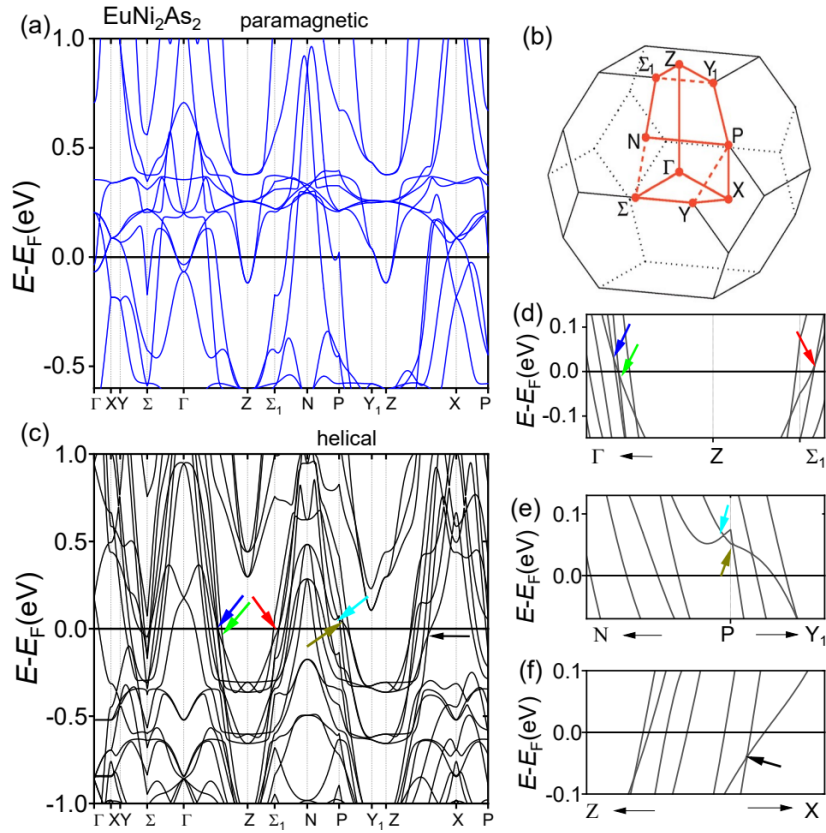


FIG. 6. The electronic band structure of EuNi_2As_2 , calculated with Coulomb correlation potential $U=5\text{ eV}$ and Hund's coupling $J=0.8\text{ eV}$, (a) for the paramagnetic state and (c) for the helical AFM state. (b) The sketch of the Brillouin zone for the $I4/mmm$ space group, with high symmetry lines shown in red. (d-f) Magnified regions of the band structure shown in (c) near the Fermi level ($E=0$).

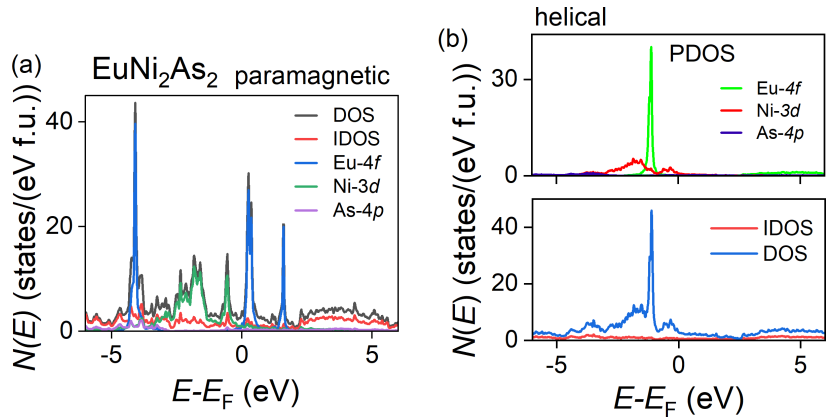


FIG. 7. Interstitial (IDOS), and total (DOS) density of states: (a) for the paramagnetic and (b) for the helical AFM phase. The PDOS shown in (b) are sums of the identical spin-up and spin-down contributions.

the conductivity at low temperatures, whereas the single band model fits very well at higher temperatures, resulting in the carrier concentration of the order of 10^{22} cm^{-3} . Probably that is why, unlike in the EuCuAs [11], the topological Hall effect was not observed in EuNi_2As_2 . The component of THE due to the Berry curvature in momentum-space brought by plausible Dirac/Weyl

points is obscured by the large concentration of carriers from topologically trivial bands, making the overall Hall resistivity very low. Survey of literature showed that usually the ρ_{xy} due to THE is a few percent of the total Hall resistivity [7]. Therefore, for EuNi_2As_2 it might be expected about $10^{-7}\Omega\text{ cm}$, which is beyond the sensitivity of our measurements.

TABLE I. Relative energies of the system ($E - E_0$), total densities of states at E_F , screened length and magnetic moments of Eu^{2+} ions calculated with the LSDA+U approach. E_0 denotes the energy calculated with $U = 0$.

| U (eV) | 5 | 5.5 | 6 | 6.5 | 7 | 7.5 | 8 |
|--------------------------------|--------|--------|--------|--------|--------|--------|--------|
| $(E - E_0)$ (meV) | -15.73 | -15.58 | -15.44 | -15.31 | -15.19 | -15.07 | -14.96 |
| $N(E_F)$ (state/(eV f.u.)) | 2.708 | 2.722 | 2.802 | 2.73 | 2.756 | 2.791 | 2.803 |
| screening length (λ) | 2.37 | 2.19 | 2.03 | 1.89 | 1.76 | 1.65 | 1.55 |
| magn. moment (μ_B /f.u.) | 6.988 | 6.999 | 7.009 | 7.018 | 7.026 | 7.034 | 7.041 |

We also revisited the specific heat with employing the Debye-Einstein model, and found characteristic parameters, which are given in Supplemental Materials [15]. Further, we incorporated the *ab-initio* calculations, which provided deeper insight into electronic band structure of the compound. The changes in the density of states, magnetic moments, and screening lengths of Eu-4*f* orbitals were discussed in terms of the effects of Hubbard corrections. We found that interstitial DOS

has a significant role in total DOS. Despite strong shift in position of Eu-4*f* band occurring with the magnetic ordering, the density of states at the Fermi level decreases only by a factor smaller than two.

ACKNOWLEDGMENT

This study was supported by the National Science Centre (Poland) under grant 2021/41/B/ST3/01141.

-
- [1] N. P. Armitage, E. J. Mele, and A. Vishwanath, Weyl and Dirac semimetals in three-dimensional solids, *Rev. Mod. Phys.* **90**, 015001 (2018).
- [2] X. Chen, S. Dong, and Z.-C. Wang, Recent advances in understanding and manipulating magnetic and electronic properties of EuM_2X_2 ($M=\text{Zn}, \text{Cd}$; $X=\text{P}, \text{As}$), *J. Phys.: Cond. Matt.* **37**, 033001 (2025).
- [3] M. C. Rahn, J. R. Soh, S. Francoual, L. S. Veiga, J. Stremper, J. Mardegan, D. Y. Yan, Y. F. Guo, Y. G. Shi, and A. T. Boothroyd, Coupling of magnetic order and charge transport in the candidate Dirac semimetal EuCd_2As_2 , *Phys. Rev. B* **97**, 214422 (2018).
- [4] J. Z. Ma, S. M. Nie, C. J. Yi, J. Jandke, T. Shang, M. Y. Yao, M. Naamneh, L. Q. Yan, Y. Sun, A. Chikina, V. N. Strocov, M. Medarde, M. Song, Y. M. Xiong, G. Xu, W. Wulfhekel, J. Mesot, M. Reticcioli, C. Franchini, C. Mudry, M. Müller, Y. G. Shi, T. Qian, H. Ding, and M. Shi, Spin fluctuation induced Weyl semimetal state in the paramagnetic phase of EuCd_2As_2 , *Sci. Adv.* **5**, eaw4718 (2019).
- [5] J. R. Soh, C. Donnerer, K. M. Hughes, E. Schierle, E. Weschke, D. Prabhakaran, and A. T. Boothroyd, Magnetic and electronic structure of the layered rare-earth pnictide EuCd_2Sb_2 , *Phys. Rev. B* **98**, 064419 (2018).
- [6] F. Gul, O. Pavlosiuk, T. Romanova, D. Kaczorowski, and P. Wiñiewski, Origin of the large topological Hall effect in the EuCd_2Sb_2 antiferromagnet, *Phys. Rev. B* **113**, 085133 (2026).
- [7] K. Singh, O. Pavlosiuk, S. Dan, D. Kaczorowski, and P. Wiñiewski, Large unconventional anomalous Hall effect arising from spin chirality within domain walls of an antiferromagnet EuZn_2Sb_2 , *Phys. Rev. B* **109**, 125107 (2024).
- [8] J. Yan, Z. Z. Jiang, R. C. Xiao, W. J. Lu, W. H. Song, X. B. Zhu, X. Luo, Y. P. Sun, and M. Yamashita, Field-induced topological Hall effect in antiferromagnetic axion insulator candidate EuIn_2As_2 , *Phys. Rev. Res.* **4**, 013163 (2022).
- [9] K. Singh, J. Skolimowski, G. Cuono, R. M. Sattigeri, A. Ptok, O. Pavlosiuk, T. Romanova, T. Toliński, P. Wiñiewski, C. Autieri, and D. Kaczorowski, Nature of field-induced transitions and hysteretic magnetoresistance in the noncollinear antiferromagnet EuIn_2As_2 , *Phys. Rev. B* **112**, 134440 (2025).
- [10] J.-R. Soh, I. Sánchez-Ramírez, X. Yang, J. Sun, I. Zivkovic, J. A. Rodríguez-Velamazán, O. Fabelo, A. Stunault, A. Bombardi, C. Balz, M. D. Le, H. C. Walker, J. H. Dil, D. Prabhakaran, H. M. Rønnow, F. de Juan, M. G. Vergniory, and A. T. Boothroyd, Weyl metallic state induced by helical magnetic order, *npj Quantum Mater.* **9**, 7 (2024).
- [11] S. Roychowdhury, K. Samanta, P. Yanda, B. Malaman, M. Yao, W. Schnelle, E. Guilmeau, P. Constantinou, S. Chandra, H. Borrmann, M. G. Vergniory, V. Strocov, C. Shekhar, and C. Felser, Interplay between Magnetism and Topology: Large Topological Hall Effect in an Antiferromagnetic Topological Insulator, EuCuAs , *J. Am. Chem. Soc.* **145**, 12920 (2023).
- [12] N. S. Sangeetha, V. Smetana, A. V. Mudring, and D. C. Johnston, Helical antiferromagnetic ordering in $\text{EuNi}_{1.95}\text{As}_2$ single crystals, *Phys. Rev. B* **100**, 094438 (2019).
- [13] W. T. Jin, N. Qureshi, Z. Bukowski, Y. Xiao, S. Nandi, M. Babij, Z. Fu, Y. Su, and T. Brückel, Spiral magnetic ordering of the Eu moments in EuNi_2As_2 , *Phys. Rev. B* **99**, 014425 (2019).
- [14] V. H. Tran, T. L. Mai, M. Sahakyan, and Z. Bukowski, First-principles study on structural, magnetic and electronic properties of $\text{EuFe}_{(2-x)}\text{Ni}_x\text{As}_2$ solid solutions, *Low Temp. Phys.* **51**, 1172 (2025).
- [15] Supplemental Material contains results on: crystal growth and characterization, heat capacity, as well as

- resistivities and de Gennes-Friedel modeling of magnetoresistance.
- [16] G. Kresse and D. Joubert, From ultrasoft pseudopotentials to the projector augmented-wave method, *Phys. Rev. B* **59**, 1758 (1999).
 - [17] J. P. Perdew, A. Ruzsinszky, G. I. Csonka, O. A. Vydrov, G. E. Scuseria, L. A. Constantin, X. Zhou, and K. Burke, Restoring the density-gradient expansion for exchange in solids and surfaces, *Phys. Rev. Lett.* **100**, 136406 (2008).
 - [18] E. Wimmer, H. Krakauer, M. Weinert, and A. J. Freeman, Full-potential self-consistent linearized-augmented-plane-wave method for calculating the electronic structure of molecules and surfaces: O₂ molecule, *Phys. Rev. B* **24**, 864 (1981).
 - [19] The ELK code. An all-electron full-potential linearized augmented plane, ver. 8.8.26, available under GNU General Public License.
 - [20] J. P. Perdew and Y. Wang, Accurate and simple analytic representation of the electron-gas correlation energy, *Phys. Rev. B* **45**, 13244 (1992).
 - [21] P. G. de Gennes and J. Friedel, Anomalies de résistivité dans certains métaux magnétiques, *J. Phys. Chem. Solids* **4**, 71 (1958).
 - [22] É. du Trémolet de Lacheisserie, D. Gignoux, and M. Schlenker, Magnetic Resistivity Magnetoresistance, and the Hall Effect, in *Magnetism - Fundamentals, Materials and Applications*, edited by É. du Trémolet de Lacheisserie, D. Gignoux, and M. Schlenker (Springer, New York, 2002) Chap. 14, pp. 443–460.
 - [23] T. Shang, Y. Xu, D. J. Gawryluk, J. Z. Ma, T. Shiroka, M. Shi, and E. Pomjakushina, Anomalous Hall resistivity and possible topological Hall effect in the EuAl₄ antiferromagnet, *Phys. Rev. B* **103**, L020405 (2021).
 - [24] W. Li, J.-X. Zhu, Y. Chen, and C. S. Ting, First-principles calculations of the electronic structure of ironpnictide EuFe₂(As,P)₂ superconductors: Evidence for antiferromagnetic spin order, *Phys. Rev. B* **86**, 155119 (2012).
 - [25] U. B. Paramanik, R. Prasad, C. Geibel, and Z. Hossain, Itinerant and local-moment magnetism in EuCr₂As₂ single crystals, *Phys. Rev. B* **89**, 144423 (2014).
 - [26] H. S. Jeevan, Z. Hossain, D. Kasinathan, H. Rosner, C. Geibel, and P. Gegenwart, High-temperature superconductivity in Eu_{0.5}K_{0.5}Fe₂As₂, *Phys. Rev. B* **78**, 092406 (2008).
 - [27] A. Liechtenstein, V. I. Anisimov, and J. Zaanen, Density-functional theory and strong interactions: Orbital ordering in Mott-Hubbard insulators, *Phys. Rev. B* **52**, R5467 (1995).
 - [28] M. R. Norman, Calculation of effective Coulomb interaction for Pr³⁺, U⁴⁺, and UPt₃, *Phys. Rev. B* **52**, 1421 (1995).
 - [29] F. Bultmark, F. Cricchio, O. Grånäs, and L. Nordström, Multipole decomposition of LDA+U energy and its application to actinide compounds, *Phys. Rev. B* **80**, 035121 (2009).

Supplemental Material

Magnetotransport and electronic band structure of EuNi_2As_2 antiferromagnet

Faheem Gul, Mane Sahakiyan, Orest Pavlosiuk and Piotr Wiśniewski

¹*Institute of Low Temperature and Structure Research, Polish Academy of Sciences, Wrocław, Poland*

(Dated: July 7, 2026)

S1. CRYSTAL GROWTH AND CHARACTERIZATION

Single crystals of EuNi_2As_2 were grown using the Bi-flux technique. Eu, Ni, As, and Bi were taken in 1:2:2:10 molar ratios. The elements were put into an alumina crucible, vacuumed and sealed in a quartz ampule. The ampule was heated to 530°C at the rate of $25^\circ\text{C}/\text{h}$, followed by a 24 hours dwell. Next, temperature was raised to 1050°C and kept for 24 hours for complete homogenization. Then the ampule was cooled to 500°C at $2^\circ\text{C}/\text{h}$ rate. Finally, platelet-like crystals were separated from flux with a centrifuge. Figs. S1(a) and S1(b) show scanning electron microscope (SEM) image, elemental composition, and a Laue diffraction pattern of a single crystal of EuNi_2As_2 , respectively.

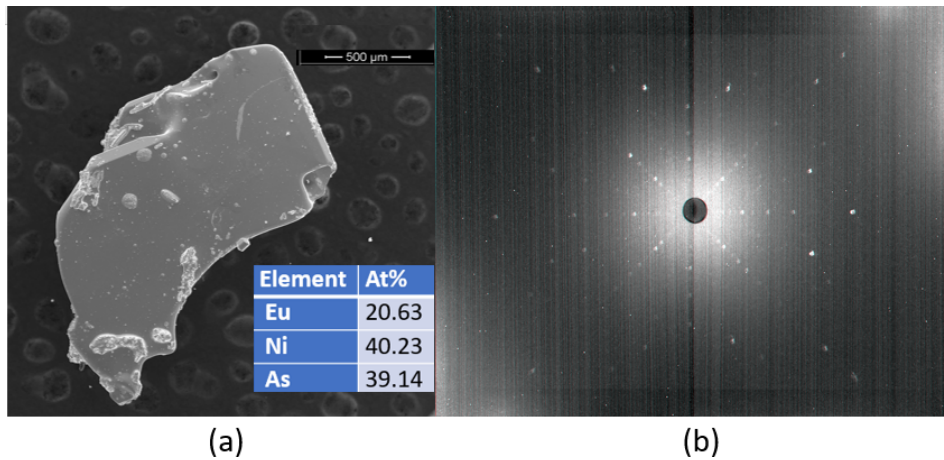


FIG. S1. (a) SEM image of a single crystal of EuNi_2As_2 . The inset shows elemental composition from EDS analysis. (b) Laue diffraction pattern taken with incident x-ray beam close to the $[001]$ crystallographic direction.

S2. HEAT CAPACITY

The specific heat (C_p) of EuNi_2As_2 was measured in the temperature range $2 \leq T < 300\text{ K}$, shown in Fig. S2. The λ -shaped anomaly associated with AFM transition is visible near $T = 14.6\text{ K}$ and shown enlarged in the inset of Fig. S2. C_p attains the classical Dulong-Petit limit just close to the $T = 250\text{ K}$, that is $3n\mathcal{R} = 124.7\text{ J mol}^{-1}\text{K}^{-1}$, where n is the number of atoms in the primitive unit cell and \mathcal{R} is the universal gas constant. To estimate the magnetic contribution to specific heat, C_{mag} , from C_p , the Debye-Einstein model was used:

$$C_p = C_{\text{mag}} + C_e + pC_E + (1 - p)C_D, \quad (\text{Eq. S1})$$

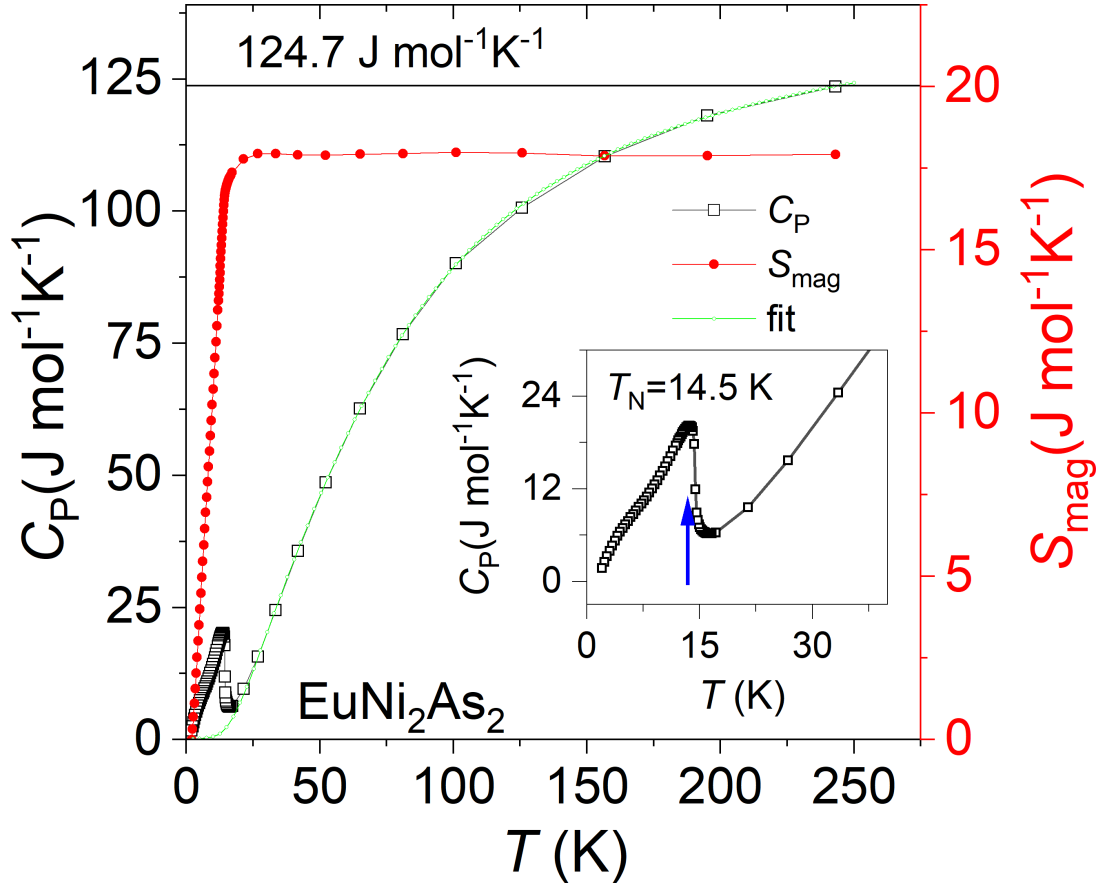


FIG. S2. The temperature dependence of the specific heat (C_p - left axis) and the magnetic entropy (S_{mag} - right axis) of EuNi_2As_2 . The green solid line shows the fit with Debye-Einstein model. The inset shows anomaly of C_p at $T_N=14.5$ K.

where C_e is the electronic contribution, C_E and C_D are the Einstein and Debye terms, respectively, and p describes the relative weight of the Einstein and Debye contribution to the C_p , and $C_e = \gamma T$, where γ is the Sommerfeld coefficient. The Debye and Einstein terms account for contributions from the acoustic and optical phonons, respectively:

$$C_D = 9n\mathcal{R} \left(\frac{T}{\theta_D} \right)^3 \int_0^{\theta_D/T} \frac{x^4 e^x}{(e^x - 1)^2} dx, \quad \text{and} \quad C_E = 3n\mathcal{R} \left(\frac{\theta_E}{T} \right)^2 \frac{e^{\theta_E/T}}{(e^{\theta_E/T} - 1)^2}.$$

θ_D and θ_E denote characteristic Debye and Einstein temperatures, respectively. The fit (solid green line) shown in Fig. S2 yielded the following parameters: $\theta_D=364(9)$ K, $\theta_E=119(3)$ K, $\gamma=31(1)$ mJ mol $^{-1}$ K $^{-2}$ and $p=0.40(3)$. The magnetic contribution C_{mag} was used to estimate the magnetic entropy as $S_{\text{mag}} = \int_{2\text{K}}^T (C_{\text{mag}}/T') dT'$. At $T = 29$ K, S_{mag} attains the maximum value of 17.9 J mol $^{-1}$ K $^{-1}$, only slightly different from the theoretical value for the Eu^{2+} ion, calculated as $\mathcal{R} \ln(2s + 1) = 17.3$ J mol $^{-1}$ K $^{-1}$ with $s = 7/2$, shown on the right axis of Fig. S2. In the previous report only the Debye model was employed, and yielded $\theta_D=280$ K and significantly lower $S_{\text{mag}}=15.38$ J mol $^{-1}$ K $^{-1}$ [12].

Furthermore, we estimated the density of states at the Fermi level, $N(E_F)$, using the γ value and the formula: $N(E_F) = 3\gamma/(2\pi^2 k_B \mathcal{N})$, where k_B denotes the Boltzmann constant and \mathcal{N} is the Avogadro number. The obtained

value is $N(E_F) \approx 14 \text{ state}/(\text{eV f.u.})$, which corresponds to the metallic nature of the EuNi_2As_2 . Moreover, the Fermi energy can be written as, $E_F = 3n/2\text{DOS}(E_F)$, where n , is the carrier concentration. For $T = 10$ and 50 K , n is $3.9 \times 10^{22} \text{ cm}^{-3}$ and $6.1 \times 10^{22} \text{ cm}^{-3}$, respectively. The resulting E_F changes from 0.7 eV at 10 K to 1.1 eV at 50 K .

S3. RESISTIVITIES AND DE GENNES-FRIEDEL MODELING OF MAGNETORESISTANCE.

The temperature-dependent resistivity ($\rho_{xx}(T)$) is shown in Fig. S3(a), with its inset showing the data in low-temperature region. The residual resistivity ratio $\text{RRR} = \rho(25 \text{ K})/\rho(300 \text{ K}) \approx 4.1$ reflects the high quality of synthesized single crystals. The field-dependent resistivity ($\rho_{xx}(H)$) is shown in Fig. S3(b) for various temperatures.

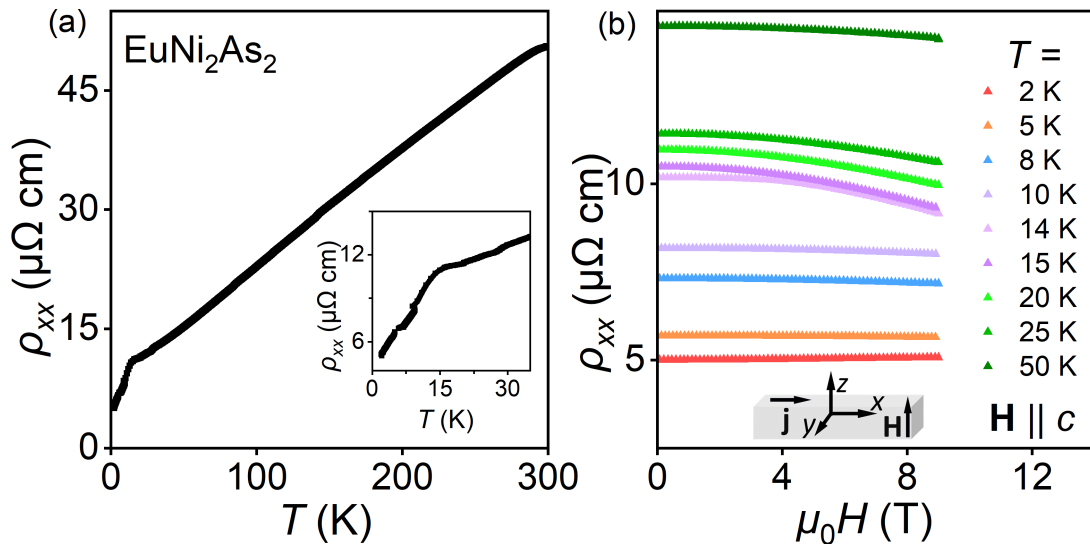


FIG. S3. (a) The temperature and (b) magnetic field dependence of the ρ_{xx} .

The suppression of spin-disorder scattering as spins get gradually aligned in the applied magnetic field, leads to negative magnetoresistivity. The mechanism was proposed by the de Gennes and Friedel [21], who proposed that the magnetoresistance reflects the field variations in the correlation function between spins, $\langle \mathbf{S}_i \cdot \mathbf{S}_j \rangle$, through the relation $\rho_{xx} \propto [S(S+1) - \langle \mathbf{S}_i \cdot \mathbf{S}_j \rangle]$. In the paramagnetic state it is related to the magnetization: $\rho_{xx}(H) \propto [1 - M^2(H)]$ [22]. For magnetic moments of Eu^{2+} we can very well approximate $M(H)$ with Brillouin function and get:

$$\rho_{xx}(T, H) = a[1 - \{m_T \tanh(H/t)\}^2] \quad (\text{Eq. S2})$$

where a denotes the ρ_{xx} at zero field, t determines the saturation field and m_T scales the magnetization (which corresponds to the term in curly brackets). This model does not fit in the helical AFM region, where strong antiferromagnetic exchange interactions enter the correlation function, and $\langle \mathbf{S}_i \cdot \mathbf{S}_j \rangle / (S(S+1))$ no longer corresponds to M^2 . The fits of Eq. S2 for various temperatures in the paramagnetic region are shown in Fig. 4 of the main text, and the fit parameters are collected in Table S1.

TABLE S1. Parameters obtained from fitting of the dGF model to $\rho_{xx}(H)$ isotherms above the Néel temperature.

| T (K) | a ($\mu\Omega$ cm) | m_{T} | t (T) |
|---------|-----------------------|----------------|----------|
| 15 | 10.4915(2) | 1.18(1) | 30.6(3) |
| 20 | 10.96672(9) | 0.7302(1) | 20.38(5) |
| 25 | 11.42224(8) | 0.689(2) | 22.01(7) |
| 50 | 14.47652(3) | 0.547(2) | 31.0(1) |